1

Experimental and simulation study of impurity transport response to RMPs in RF-heated H-mode plasmas at EAST

Germán Vogel [1,2], **Hongming Zhang**[1], **Yongcai Shen**[3], **Shuyu Dai** [4],
Youwen Sun[1], **Juan Huang**[1], **Shuai Gu**[1], **Jia Fu**[1], **Ruiji Hu**[1,2], **Jun Chen**[1,2],
Xuewei Du[5], **Qiuping Wang**[5], **Yi Yu**[2], **Shifeng Mao**[2], **Bo Lyu** [1,†]
and **Minyou Ye**[2,†]

[1]Institute of Plasma Physics, Chinese Academy of Sciences, Hefei 230031, PR China

[2]School of Nuclear Science and Technology, University of Science and Technology of China,
Hefei 230026, PR China

[3]School of Physics and Materials Engineering, Hefei Normal University, Hefei 230601, PR China

[4]Key Laboratory of Materials Modification by Laser, Ion and Electron Beams (Ministry of Education),
School of Physics, Dalian University of Technology, Dalian 116024, PR China

[5]National Synchrotron Radiation Laboratory, University of Science and Technology of China,
Hefei 230029, PR China

Spatial profiles of impurity emission measurements in the extreme ultraviolet (EUV) spectroscopic range in radiofrequency (RF)-heated discharges are combined with one-dimensional and three-dimensional transport simulations to study the effects of resonant magnetic perturbations (RMPs) on core impurity accumulation at EAST. The amount of impurity line emission mitigation by RMPs appears to be correlated with the ion Z for lithium, carbon, iron and tungsten monitored, i.e. stronger suppression of accumulation for heavier ions. The targeted effect on the most detrimental high-Z impurities suggests a possible advantage using RMPs for impurity control. Profiles of transport coefficients are calculated with the STRAHL one-dimensional impurity transport code, keeping v/D fixed and using the measured spatial profiles of Fe^{20+}, Fe^{21+} and Fe^{22+} to disentangle the transport coefficients. The iron diffusion coefficient D_{Fe} increases from $1.0 - 2.0$ m^2 s^{-1} to $1.5 - 3.0$ m^2 s^{-1} from the core region to the edge region ($\rho > 0.5$) after the onset of RMPs. Meanwhile, an inward pinch of iron convective velocity v_{Fe} decreases in magnitude in the inner core region and increases significantly in the outer confined region, simultaneously contributing to preserving centrally peaked Fe profiles and exhausting the impurities. The D_{Fe} and v_{Fe} variations lead to reduced impurity contents in the plasma. The three-dimensional edge impurity transport code EMC3-EIRENE was also applied for a case of RMP-mitigated high-Z accumulation at EAST and compared to that of low-Z carbon. The exhaust of C^{6+} toward the scrape-off layer accompanying an overall suppression of heavier W^{30+} is observed when using RMPs.

Key words: fusion plasma, plasma diagnostics, plasma simulation

---

† Email addresses for correspondence: blu@ipp.ac.cn, yemy@ustc.edu.cn

1. Introduction

Impurity radiation power losses in fusion plasmas are a major obstacle to achieving steady-state operation in magnetic confinement devices. This is all the more pressing as ITER and DEMO reactors consider the use of high-Z materials for their plasma-facing components (PFCs), such as full tungsten divertors and iron and molybdenum from austenitic steel 316LN on the vacuum vessel first wall (Hirai *et al.* 2014; Merola *et al.* 2014). Once eroded from the PFC and ionized upon interaction with the surrounding plasma, the impurities accumulate in the core region where they contribute dramatically to radiative cooling and to disruptions during high-confinement mode (H-mode) operation. An appropriate technique of impurity control must address both problems: avoid the wear of PFC releasing heavy ions into the plasma and provide a mechanism for reducing their concentration at the core.

Resonant magnetic perturbations (RMPs) have become commonplace for mitigating the relaxation events known as edge localized modes (ELMs) since being demonstrated in H-mode plasmas at DIII-D in 2004 (Evans *et al.* 2004). The mitigation of these bursting instabilities with a high energy-transfer rate is key to avoid damage on the surrounding PFCs. More recently, the observation of low-Z impurity emissions using interferometry measurements whereas applying RMPs has shown a decrease of effective charge, Z_{eff} (Fischer *et al.* 2011), the targeted exhaust of impurity He ions toward the scrape-off layer (SOL), and the decrease of He confinement time when compared with the main ions (Schmitz *et al.* 2016). The results suggested an RMP effect going beyond the avoidance of PFC erosion. In fact, RMP studies at the Experimental Advanced Superconducting Tokamak (EAST) have shown that increasing the RMP current, I_{RMP}, modifies the edge magnetic field layer topology by decreasing the connection length of magnetic field lines in that region (Sun *et al.* 2015). It is then interesting to study the associated impurity transport mechanisms which link these modifications to a targeted effect of RMPs on impurities.

EAST provides an ideal testing ground with enhanced capability for steady-state H-mode operation owing to its superconducting magnets, an array of RMP coils capable of mitigating and fully suppressing ELMs (Sun *et al.* 2016), a tungsten upper divertor and vacuum vessel materials which are sources of iron and molybdenum. The present work reports on the profile measurement of partially ionized low- and high-Z impurities under the influence of RMP fields, using extreme ultraviolet (EUV) spectroscopy to access the core region. For EAST H-mode discharges, impurity emission profiles are compared for cases before and during the application of RMPs. The aim is to provide insights as to how the perturbation fields and the mitigation of ELMs affect the accumulation of unwanted impurity ions in the plasma. Combining the impurity emission profiles measurements with STRAHL (one-dimensional) and EMC3-EIRENE (three-dimensional) transport codes, has helped investigate both the role of RMPs for impurity control and the processes associated.

2. Experimental data acquisition

Figure 1 shows the set-up of the space-resolved EUV spectrometer installed at the end of an 8.3 m long vacuum duct of port-C at EAST. It observes the plasma in the vertical direction between 0 and 450 mm (from the midplane up) at $R_{ax} = \sim 1.85$ m. The EUV spectrometer consists of a slit assembly (a variable-width entrance slit and a space-resolving slit), a 1200 grooves mm^{-1} varied line-spaced (VLS) grating and a CCD detector. Typical time resolutions of 20 ms are obtained with full vertical binning (FVB) of the CCD 2048 × 2048 pixels array. A spatial resolution of 45 mm is achieved when the
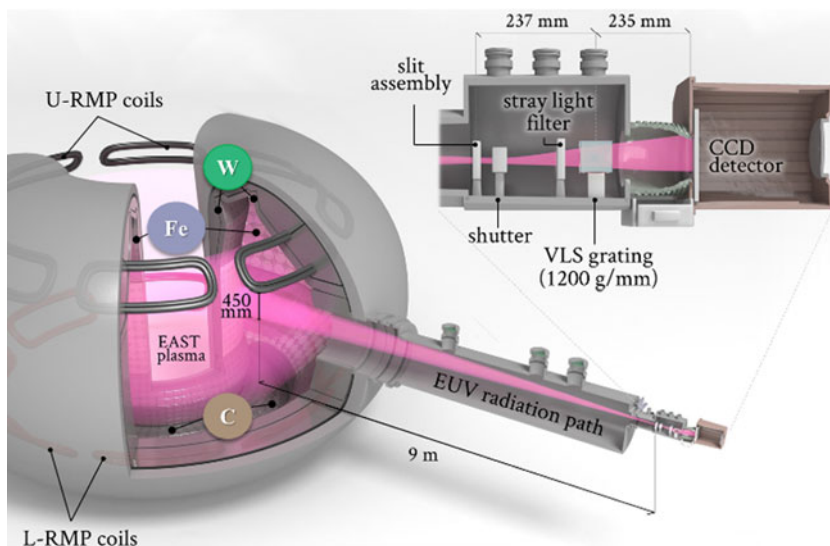
FIGURE 1. Components of EUV spectrometer and set-up with respect to the EAST plasma and relevant impurity sources: tungsten/carbon from the upper/lower divertor and iron from the vessel walls.

space-resolved slit width is set to 1 mm and 100 pixels of sensing surface are binned for a single channel.

Routine operation is under high vacuum of around 10^{-5} Pa to avoid EUV radiation absorption by air molecules. Orienting the VLS grating at an incident angle of $87°$ produces near flat-field spectral images in the wavelength range 3–50 nm recorded by the CCD with a spectral resolution of 0.006 nm. An absolute intensity calibration was carried out at the National Synchrotron Radiation Laboratory of the University of Science and Technology of China, and a detailed description of the spectrometer can be found in Shen *et al.* (2013).

The acquired spectra look like those shown in figure 2. The figure shows some of the prominent lines of typical H-mode discharges at EAST and highlights the capacity of the spectrometer to capture spatially resolved measurements (in the poloidal z-direction). The spectrum varies from around the midplane $z_1 = 0$ mm to the highest observable position $z_3 = 450$ mm. The wavelength range can be shifted up to 50 nm with the help of a motorized stage mounted on the CCD detector to scan the full spectra refracted from the grating.

For the aims of the present work, the emissions of $n = 2p \rightarrow 1s$ transition lines of C^{6+} (3.37 nm) from the carbon lower divertor of EAST and Li^{2+} (13.50 nm) from wall conditioning were separately resolved and measured by the EUV spectrometer. This serves the double purpose of contrasting their behaviour with that of high-Z impurities and for real-time calibration of emission lines position.

At the usual central electron temperatures of EAST between $0.5-2$ keV, high-Z impurity ions are still only partially ionized. A prominent line of ionized iron (Fe^{22+}) eroded from the stainless-steel PFC of the vacuum vessel appears in the EUV spectra at 13.29 nm for the $2s2p \rightarrow 2s^2$ transition. Tungsten from the upper divertor is monitored through its unresolved transition array (W-UTA) between 4.8$-$5.3 nm, which contains ionization states W^{26+} to W^{30+}.

An RMP coil system (Wan *et al.* 2017) has been installed at EAST and used since the 2014 experimental campaign allowing magnetohydrodynamic (MHD) control and physics
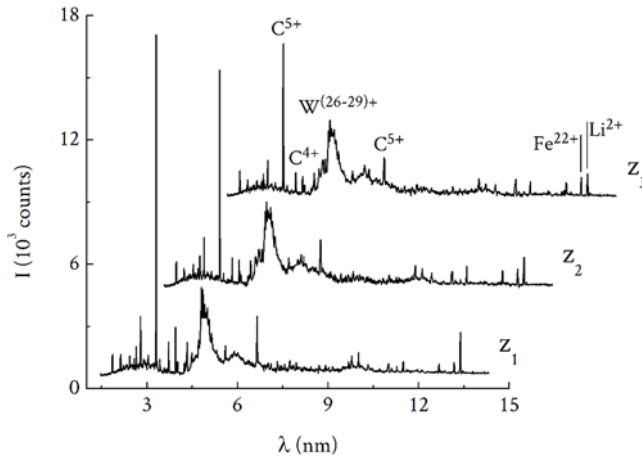
FIGURE 2. Segments of spatially resolved EAST EUV spectra recording impurity emission lines of carbon, tungsten, iron and lithium during the plateau of discharge #67578, at three different vertical positions $z_1 (\sim 0$ mm$)$ to $z_3 (\sim 450$ mm$)$.

studies. The RMP system, also illustrated in figure 1, consists of 16 coils arranged in two symmetric upper and lower arrays (RMP$_U$, RMP$_L$) at the EAST low-field side (LFS). Each coil, which covers 2 of the 16 ports of EAST, consists of 4 turns and can circulate up to $I_{RMP} = 12$ kA. The location of the RMP coils toroidal angle $\varphi = 0$ is defined as the centre of the coils covering the P and A ports of EAST. The geometry of the arrays along the toroidal direction is not continuous and RMP coil current can be applied at a given phase, so it is normal to expect a non-symmetric distribution of impurities dependent on φ, and a more symmetrical distribution when RMPs are not present.

Figure 3 shows the waveforms of a 20 s long RF-heated EAST pulse #67578, with plasma current $I_P = 450$ kA and heating power $P_{RF} = P_{ECRH} + P_{ICRF} = 1.0$ MW and $P_{LHW} = 2.2$ MW. The time evolution of impurity intensities is presented in figure 3(h). During a first stage before $t = 2.0$ s (first dashed line and arrow), as I_P increases, the LHW heating and supersonic molecular beam injection (SMBI) fuelling are switched on leading to an increase in n_e and to the introduction of iron and carbon into the main plasma.

In a second stage $2.0 < t < 3.2$ s, the ECRH and ICRF heating systems are turned on, and as the D_α signal indicates the onset of an ELMy H-mode regime, all impurity emissions monitored rise dramatically possibly due to ELM-caused particle and heat deposition on the PFC. Figure 3(h) corresponds to the line emissions from the EUV spectrometer, with a time resolution of 20 ms, which allows adequately resolving the impurity decay time typically longer than 100 ms. The plasma parameters during this stage are labelled 'no-RMP' and serve as the comparison with the stage previous to the onset of RMP, with plasma parameters at this stage labelled 'with-RMP'.

The RMP current rises from $t = 3.0$ s. However, significant plasma response to RMP occurs at $t = 3.2$ s (second dashed line and arrow), when I_{RMP} reaches 1 kA. At this point, the ELMs are abruptly mitigated and the stored energy decreases slightly by 15 %, by a typically observed effect of pump-out when RMPs are used. Most remarkably, the W emissions in the core are reduced dramatically. The discharge becomes stable at about $t = 4.0$ s. The W emission with RMP at this stage sees a decrease of about 70 % with respect to that without RMP ($t = 3.0$ s). In comparison, C^{6+} emissions see a modest decline of 20 %. Although Fe^{22+} had peaked and started to go down in the previous stage in apparent response to the increased RF heating, its intensity experiences a 50 %
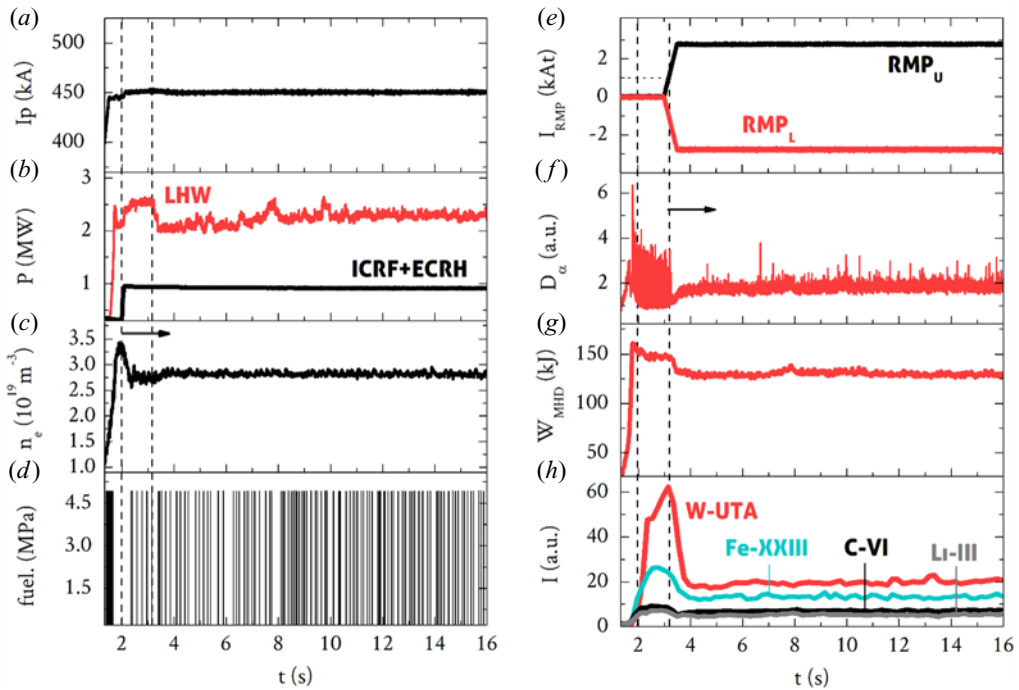
EAST #67578

FIGURE 3. Time evolution of (*a*) plasma current, (*b*) LHW and RF (ICRF + ECRH) heating power, (*c*) electron density, (*d*) SMBI fuelling, (*e*) RMP coil current, (*f*) D, (*g*) stored energy and (*h*) impurity line emissions of W-UTA, Fe^{22+} and C^{5+}, showing a marked decrease after I_{RMP} reaches about 1 kAt and mitigates ELMs at $t = 3.2$ s (second dashed line and arrow).

mitigation with RMP. The mitigation of high-Z impurity emissions seems to be related to I_{RMP} rather than to variations in n_e, T_e or W_{MHD} which only change modestly. Even the spatial profiles of n_e, T_e from the TS diagnostic (Zang *et al.* 2010) and T_i from XCS (Lyu *et al.* 2014, 2016), shown in figure 4, do not appear to account for the mitigation levels, with n_e, T_e slightly increasing with RMP (particularly more so in central plasma regions) and T_i staying relatively the same.

Figure 5 shows the relative reduction of emissions of the different impurities surveyed in response to the use of RMPs. This suppression of impurity accumulation at the core increases with the impurity ion mass, which hints at an additional transport process on top of the usual inertial particle pump-out effect routinely observed with RMP. The latter would exhibit an approximately an equal or a more pronounced effect on low-Z impurities, so the observations from figure 5 point to a targeted effect on higher-Z impurity ions. A cross-field transport process related to the differences of the impurities gyroradii, as has been observed by Zhang *et al.* (2017) in LHD, could explain the different responses, although the role of the ion charge remains unclear at present.

3. Impurity transport simulation modelling

3.1. *Three-dimensional modelling with EMC3-EIRENE*

Examining the outer plasma boundary can give a complete picture of the exhaust and mitigation processes at the plasma centre, because the core region is intimately affected
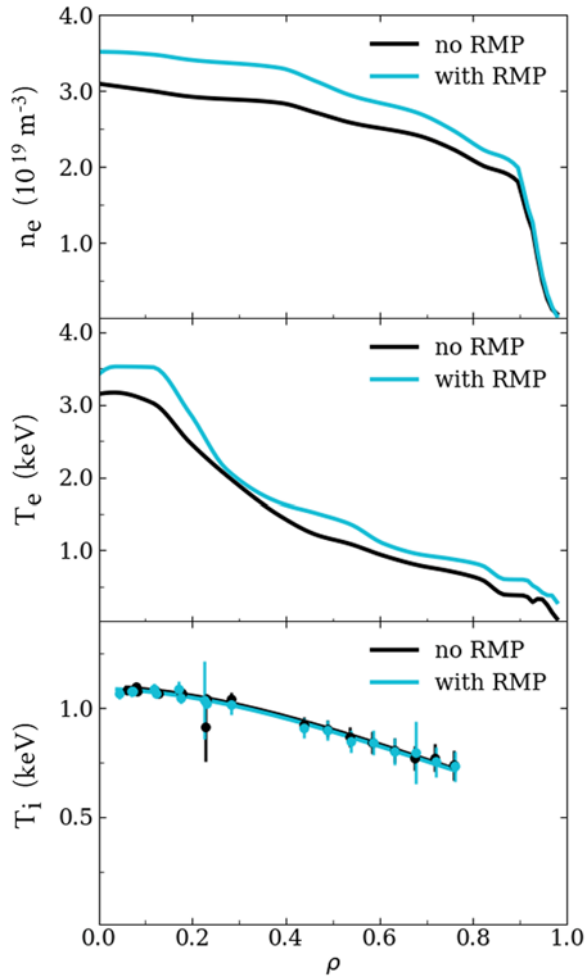
FIGURE 4. Changes of profiles of n_e, T_e (from the TS diagnostic) and T_i (from XCS) at 2.5 s (before RMP, black coloured) and at 5.5 s (during RMP, blue coloured).

by the processes occurring in the surrounding edge. The three-dimensional edge impurity transport code EMC3-EIRENE (Reiter 1992; Feng *et al.* 1997) has been used at ASDEX Upgrade (Lunt *et al.* 2012) and more recently at LHD (Zhang *et al.* 2017) to analyse the overall effects of RMPs on magnetically confined plasmas, including on low-Z impurities, and is considered in this study for this purpose.

The code package consists of a Monte Carlo fluid transport (EMC3) including kinetic particle recycling and transport (EIRENE), solving the plasma continuity, parallel momentum and energy fluid equations, while calculating the particle, momentum and energy source terms. Fluid transport is considered to be classical and parallel to the field lines. With negligible pressure gradient, electric field and electron temperature gradient forces, it is described by the momentum equation (Morita *et al.* 2013),

$$m_z \frac{\partial v_{z\parallel}}{\partial t} = m_z \frac{v_{i\parallel} - v_{z\parallel}}{\tau_{zi}} + 2.6 Z^2 \frac{\partial T_i}{\partial s}, \tag{3.1}$$
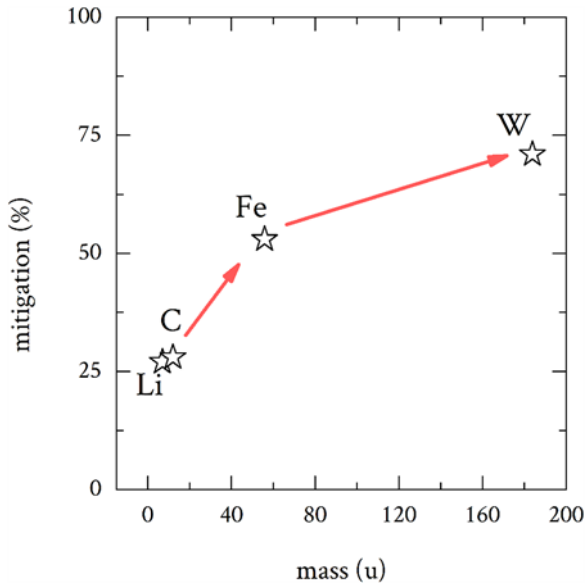
FIGURE 5. Impurities intensity amount of mitigation (per cent) increasing trend with ion mass. Updated and corrected from Vogel *et al.* (2018).

with s the coordinate along the field line, τ_{zi} the collisional time between impurity ions and background plasma ions and $v_\parallel$ the parallel velocity. The terms on the right-hand side both represent the dominant forces in the direction parallel to the magnetic field lines: a friction force (F_F) with the bulk plasma ions towards the divertors and an ion temperature gradient force (F_{ITG}) away from them. The balance between these forces determines cases in which impurities are either screened ($F_F > F_{\mathrm{ITG}}$) or build up ($F_F < F_{\mathrm{ITG}}$).

Cross-field transport, on the other hand, is assumed to be diffusive with anomalous coefficients of heat conductivity ($\chi_\perp$) and bulk particle and impurity diffusivities ($D_\perp$ and $D_{Z\perp}$, respectively). The excitation and ionization of the impurities lead to energy sinks in the steady-state fluid equations for the particle, momentum and energy transport of ions and electrons (Dai *et al.* 2016). These energy sinks represent the impurity effects on the background plasma.

3.2. *One-dimensional modelling with STRAHL*

Collisional-radiative models (Summers *et al.* 2006) best describe the populating and depopulating processes of excited levels of impurity atoms in typical tokamak plasmas where $10^{18} \leq n_e \leq 10^{23}$ m^{-3}. They relate the emission of an impurity, ε_z, to the impurity concentration, n_z, according to

$$\varepsilon_{z,\lambda}(r) = n_z(r) \cdot n_e(r) \cdot \mathrm{PEC}_{z,\lambda}(r), \tag{3.2}$$

where the photon emission coefficients, PEC, are functions of n_e and T_e tabulated in the ADAS atomic processes database. With the diffusion coefficient, D, and convective velocity, v, as inputs, the one-dimensional impurity transport code STRAHL (Dux 2014) can solve the radial continuity equation for impurity ion densities,

$$\frac{\partial n_Z}{\partial t} = \frac{1}{r}\frac{\partial}{\partial r}r\left(D\frac{\partial n_Z}{\partial r} - v \cdot n_Z\right) + Q_Z. \tag{3.3}$$

The transport equation of each ionization state couples to the neighbouring states through the Q_Z source/sink term. Inputs for STRAHL include the tokamak geometry, atomic data such as recombination and ionization coefficients (also obtained from ADAS) and plasma parameters such as the safety factor, electron density and electron temperature.

In the present work, spatial profiles of T_e and n_e from the EAST Thomson scattering (TS) diagnostic system are used as inputs in the STRAHL modelling. Owing to the limited ADAS data available for tungsten, the transport of iron is investigated to represent the behaviour of high-Z elements. Optimizing the fitting of simulated n_z profiles to experimental emissivity data by varying the transport coefficients of (3.3) allows one to obtain the radial profiles of diffusion and convective velocity of the high-Z impurity. This method has been used to study the effects of ECRH on the transport of molybdenum at EAST (Shen *et al.* 2019), showing that the changes in ν and D can affect the density profiles of the ions. Accordingly, one emission line is used initially to determine ν/D. By fixing the ratio of transport coefficients while varying D, the impurity density profiles can be changed until reaching a best fit with the experimental results. The independent transport coefficients can be obtained when more than three successive lines are used to compare with simulated results. In a similar study of ECRH effects on carbon at HL-2A (Cui *et al.* 2013), the same method showed that as few as two successive emission lines are needed to determine ν and D if additional constraints are taken into account on the radial profiles and impurity sources.

4. Simulation results and discussion

Impurity transport studies can help discriminate whether the decrease in impurity emissions is only owed to the mitigation of ELMs, from the associated decrease in sputtering of impurities from the PFC entering the plasma, or also from an additional role of RMPs on edge impurity transport, predominantly from the nature of their modifications of the edge magnetic topology.

The T_i profiles measured by X-ray crystal spectrometer (XCS) and n_e and T_e profiles from TS diagnostics of discharge #67578 from figure 4, were used as the plasma parameters for an EMC3-EIRENE simulation, according to (3.1) as discussed in the previous section. The details of these profiles are discussed in Vogel *et al.* (2018). They show typical H-mode features such as a pedestal formation. In addition, the particle diffusion coefficient of the bulk plasma is assumed equal to that of the impurity ions, $D_\perp = D_{Z\perp} = 0.4$ m^2 s^{-1}, and a heat conductivity of $\chi_\perp = 2.0$ m^2 s^{-1} is used in the simulation for the perturbed case. Both coefficients are determined by optimizing a fit of measured n_e and T_e profiles to those simulated by EMC3-EIRENE. The code outputs the two-dimensional distribution (cross-sections) of impurity ions at four different toroidal angles, $\varphi = 0°, 90°, 180°$ and $-90°$. Figure 6 presents such a comparison in φ for high ionized stages of low- and high-Z impurities: C^{6+} and W^{30+}. Neither the impurity profiles from spectroscopy data nor the plasma response to the RMP magnetic fields are included, but the simulated impurity distribution contours of low- and high-Z impurities serves as an approximation to the expected impurity behaviour. In this case, distributions of high- to medium-ionized impurity carbon and tungsten ions are considered. The present results should be taken with a caveat: edge impurity transport and emissions could be modified from changes in the edge magnetic configuration resulting from the effects of the plasma response to the application of RMPs. Work is currently underway to include the effects of the plasma response and to validate the coefficients of impurity sputtering in the no-RMP and with-RMP cases (Dai *et al.* 2020).

The distributions ion density for C^{6+} and W^{30+}, in the order of 10^{15} m^{-3} and 10^{13} m^{-3}, respectively, are toroidally asymmetric when RMPs are applied, as shown in figure 6 and
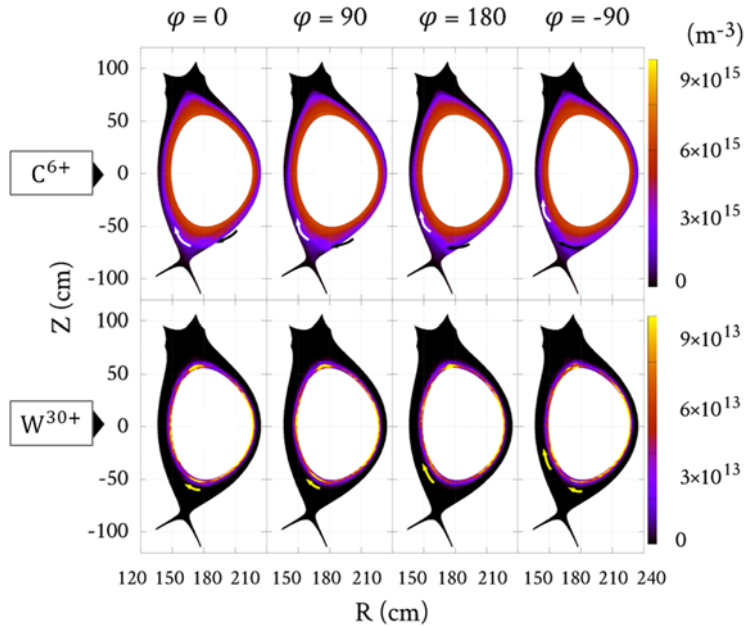
FIGURE 6. Non-symmetric toroidal phase distribution of (*a*) C^{6+} and (*b*) W^{30+} concentrations in the SOL and outer core region, in response to RMP geometry. Arrows follow the apparent clockwise rotation of blobs and filaments of higher concentration in USN configuration.

in radial profiles from it in figure 7 at $Z = -60$ cm for C^{6+} and at $Z = -52$ cm for W^{30+}. The carbon ions distribute more widely across the radius and small toroidal dependence is seen in the central region. Toroidal asymmetry is observed, however, around $R = 162$ cm and $R = 192$ cm, representing the rotating blobs indicated by arrows on the top panels of figure 6. A higher degree of toroidal asymmetry is observed for W^{30+}, with the peaking features in figure 7 representing the thinner but more abrupt blobs of higher impurity concentration which appear to rotate along the arrows on the bottom panels of figure 6.

This differs from the no-RMP case, in which no clear toroidal asymmetries are seen for either carbon or tungsten. The different response could be attributed to the discontinuous geometry of RMP coils and toroidal mode phases. It should be noted that P_{ICRF} represents only 20 % of the total heating power at the flat-top phase, $P_t = 3.2$ MW, so impurity distribution asymmetries from induced electric fields by ICRH heating are not expected. In other comparable machines, small asymmetries of tungsten associated to ICRH heating are observed in the poloidal direction with high $P_{ICRF} > 3$ MW. As tracked by arrows in figure 6, the outer boundary of the core region shows structures like blobs of higher impurity concentration, appearing to rotate clockwise near the lower divertor as one rotates toroidally around the EAST plasma volume. As this is a stationary case, the movement is just in space. Such distribution is similar for the low- and high-Z impurities, although the apparent rotation speed is slightly higher for tungsten ions.

Figure 8 shows changes in the distributions of C^{6+} and W^{30+} ion density at $\varphi = 90°$ with RMP applied. Impurities of different Z respond differently in the RMP case. The C^{6+} ion density slightly increases in the outer core, possibly from cross-field transport flushing out from the inner core regions. It decreases near the lower divertor, the source of carbon contamination and recycling. The latter suggests the dominance of F_{ITG} pushing C^{6+} ions up parallel to the field lines due to impurity buildup. Tungsten, on the
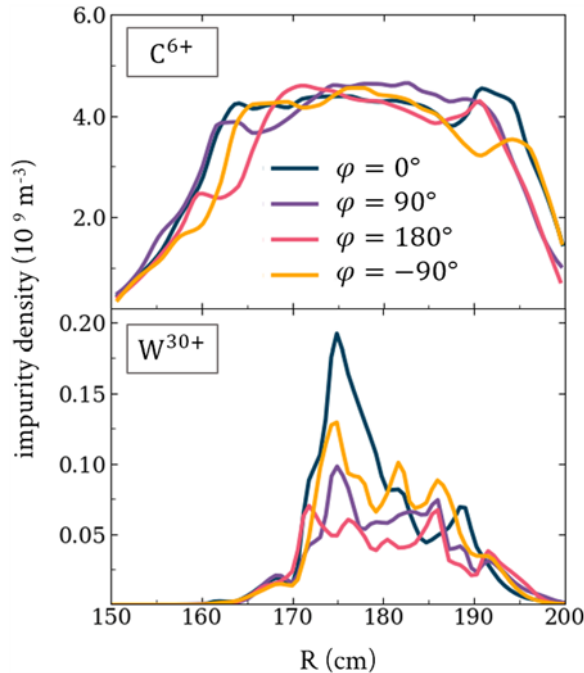
FIGURE 7. Impurity radial profiles at $Z = -60$ cm for C^{6+} and $Z = -52$ for W^{30+}, showing the asymmetric distribution of the respective ionized stages along the toroidal direction for $\varphi = 0°, 90°, 180°$ and $-90°$.

other hand, appears to be suppressed globally, with isolated filaments and islands of higher concentration remaining in the outer core region. While the impurity distributions present slight variations at different φ locations, the features described are the same in all of them. A detailed analysis on the impact of RMP on transport of carbon at the edge for the same discharge can be seen in Dai *et al.* (2020).

As cross-field transport processes, overall impurity suppression and/or radial impurity exhaust from the core are involved, a clearer picture can be obtained complementing these results with the effect of RMP on diffusive and convective radial transport processes from STRAHL.

The same background plasma parameters and profiles used for the EMC3-EIRENE simulation and spatial profiles of iron line emissions have been used in a STRAHL simulation. Iron was chosen for the high-Z impurity transport study because of the ease in interpreting a single emission line in the EUV spectra, compared with the difficulties associated with disentangling the tungsten unresolved array seen in figure 2 and figure 9 between 45 and 55 nm. The behaviours of these two high-Z impurities are not expected to differ significantly, except for a shift in their overall spatial distributions.

Figure 9 shows the three iron lines of successive ionized stages Fe^{20+}, Fe^{21+} and Fe^{22+} observable in the EUV spectra, which were monitored to study the impurity transport with STRAHL. The radial distribution of the three ionized stages of iron ions during the no-RMP and with-RMP phases for EAST discharge #67578 are compared in figure 10, where dark colours indicate the fits of EUV spectroscopy measured data to the STRAHL simulated data shown with light colours. The black lines correspond to the unperturbed profiles averaged around 2.3 and 2.5 s before the RMPs were applied, whereas the red lines represent the during the application of RMPs. Centrally peaked
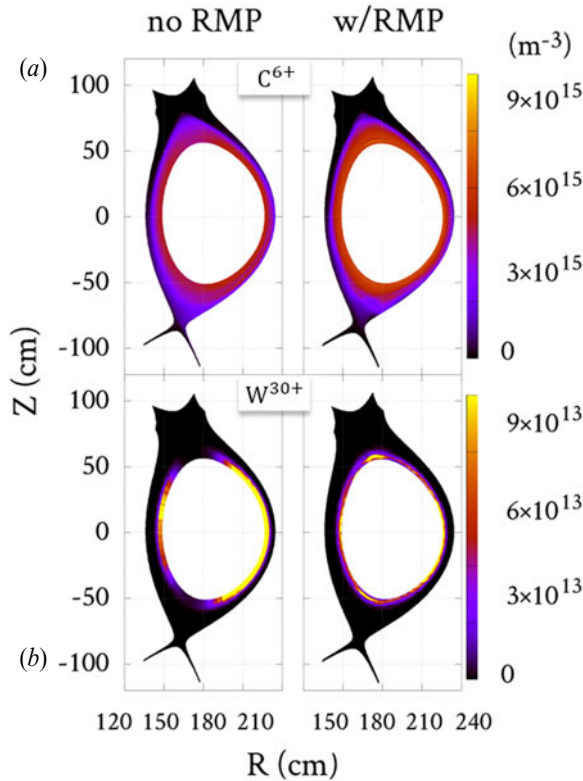
FIGURE 8. (*a*) Exhaust of C^{6+} from core to SOL and (*b*) overall decrease of W^{30+} concentration and formation of filament structures at SOL, when RMPs are injected ($\varphi = 90°$).
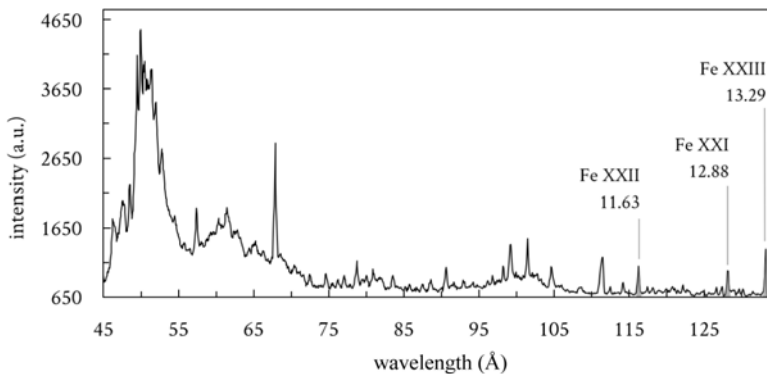

FIGURE 9. Three emission lines of successive ionized stages of iron Fe^{20+} (12.88 nm), Fe^{21+} (11.63 nm) and Fe^{22+} (13.29 nm) in the EAST EUV spectrum of discharge #67578.

profiles are seen in all cases, with impurities concentrating toward the plasma centre, as expected from the accumulation of heavy metallic ions at the plasma core routinely observed in other machines. The impurity iron spatial profiles show a significant overall decrease, particularly in the core, during the application of RMPs (red lines of figure 10). This is in agreement with the global reduction of high-Z tungsten seen in the previous
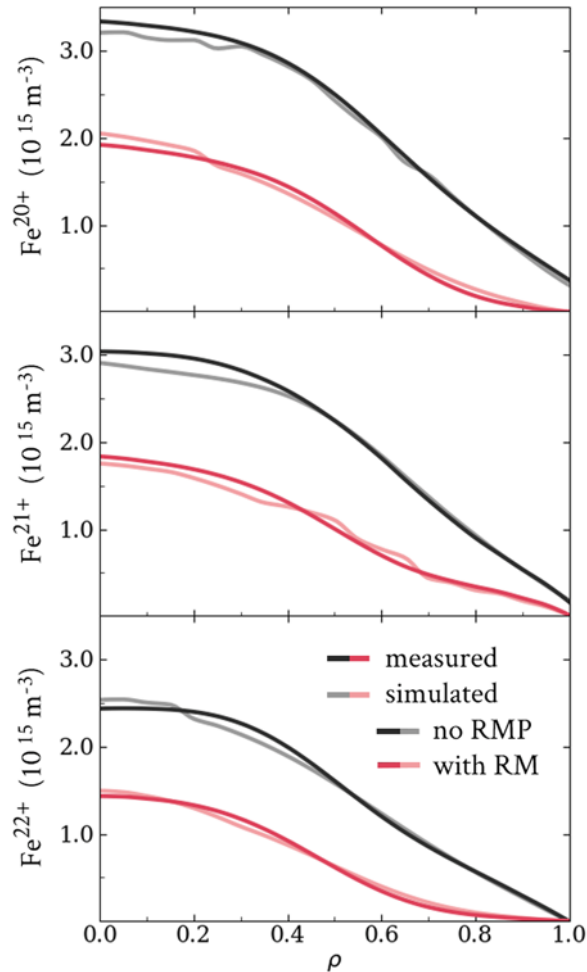
FIGURE 10. Decrease of Fe^{20+}, Fe^{21+} and Fe^{22+} spatial profiles when applying RMPs averaged around 4.0 s and 12.0 s (red lines) compared with the unperturbed profiles averaged around 2.3 and 2.5 s (black lines). Dark colours correspond to fits of the profiles measured by EUV spectroscopy to the STRAHL simulated data represented with light colours.

EMC3-EIRENE modelled results. The strong central peak of radiation is also dramatically flattened. As can be seen from the figure, the agreement reached between the measured and simulated profiles data is satisfactory.

Radial profiles of D_{Fe} and v_{Fe} ($v > 0$ defined as outward velocity) are obtained using the method discussed in § 3.2 and Shen *et al.* (2019) thanks to the EAST EUV spectrometer capacity to resolve three successive iron emission lines: Fe^{20+} at 12.88 nm, Fe^{21+} at 11.63 nm, and Fe^{22+} at 13.29 nm all shown in the spectrum of figure 10 for shot #67578. A best fit of the measured data to the simulated STRAHL data for the successive ionized stages allows obtaining distinct profiles for D_{Fe} and v_{Fe}. The spatial profiles of the transport coefficients, smoothed with a piecewise cubic Hermite interpolating polynomial, are presented between $\rho = 0.0$ and 1.0 in the top and bottom panels of figure 11, respectively. Their response to RMPs is indicated in red, contrasted to the no-RMP phase in black.
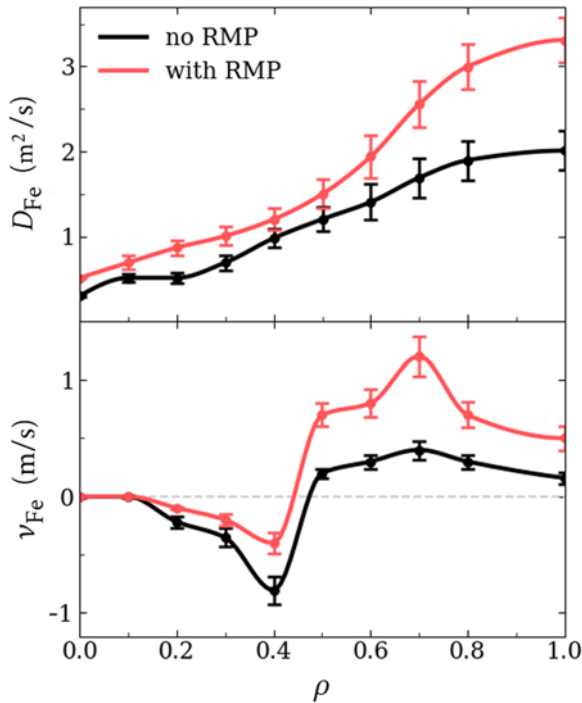
FIGURE 11. Spatial profiles of D_{Fe} and v_{Fe} transport coefficients for impurity iron calculated with STRAHL. Both diffusion and outward convection increase significantly in the outer confined region ($\rho > 0.5$) when RMPs are applied (red lines), contributing to more efficient impurity exhaust.

Both coefficients are modified, with RMP effects being more significant in the confined region at $\rho > 0.5$ all the way into the separatrix. The D_{Fe} profiles exhibit a steady increase of diffusivity from the core outward to the edge. In the with-RMP case, D_{Fe} increases by a factor of 1.5 between $\rho = 0.5 - 1.0$, from $1.0 - 2.0 \text{ m}^2 \text{ s}^{-1}$ to $1.5 - 3.0 \text{ m}^2 \text{ s}^{-1}$ with respect to that of the no-RMP scenario. This would indicate that the perturbed fields open a diffusive transport channel for the exhaust of iron out of the core by increasing values of turbulent diffusivity. It must be reminded that STRAHL is a one-dimensional code in which the plasma response is not included. However, this could nonetheless explain, at least partially, the decrease in the spatial profile. Assuming tungsten behaves in a similar way, this increased diffusivity right at the outer core could also account for the overall suppression of W^{30+} seen in figure 8.

Previous studies using a similar method to study low-Z impurity transport showed that RMPs only affect D (Greiche *et al.* 2008). In the present case, v_{Fe} also appears to be modified by the use of RMPs. As can be seen in the lower panel of figure 11, the v_{Fe} profiles in the no-RMP and with-RMP scenarios both present an inward pinch ($v_{Fe} < 0$) within the centrally confined region around $\rho = 0.4$, presumably responsible for maintaining centrally peaked profiles of iron. However, the v_{Fe} during RMP is of smaller magnitude, switching the balance toward the diffusive expulsion of impurities in that region. In the outer confined region ($\rho > 0.5$) they both invert signs (outward direction) and the RMPs cause a significant increase of outward convective velocity, with a pronounced peak at $\rho = 0.7$.

Although diffusion increases significantly toward the edge when RMPs are applied, so does the outward convective velocity, each contributing additionally to an effective exhaust of iron, as observed in the decrease of the profiles in figure 10. Both observations of impurity mitigation by EUV spectroscopy and the EMC3-EIRENE simulation seem to point at this same behaviour. This seems to be plausible considering the large and widespread increase of D_{Fe}, ν_{Fe} and the associated decrease of Fe^{22+} confinement time when RMPs are used. Meanwhile, an inward pinch of convective velocity contributes to preserve peaked iron profiles in both the no-RMP and with-RMP cases, but less efficiently so in the latter case, which can explain why the flattening of iron profiles also occurs in this region.

5. Conclusions

It has clearly been observed that RMPs drive core impurity suppression (low- and high-Z alike) in EAST, as measured by space-resolved EUV spectroscopy. The amount of impurity mitigation by RMPs is correlated with the ion mass, i.e. the heavier the ions the stronger the suppression. Such effects highlight a promising advantage of RMPs as a high-Z impurity control technique. STRAHL-calculated transport coefficients have shown both D_{Fe} and ν_{Fe} are affected by RMPs, implying a decrease of confinement time of impurity iron ions when RMPs are applied. A factor of 1.5 increase in D_{Fe} is observed from the boundary of the core region outward ($\rho > 0.5$) after the onset of RMPs. Meanwhile, ν_{Fe} shows a decrease in magnitude in the inward direction in the core, benefitting diffusive impurity exhaust from this region. A significant increase of ν_{Fe} (peaked at $\rho = 0.70$) in the outward direction is also seen with RMPs, contributing together with the larger D_{Fe} to expel impurities from the confined plasma region. These variations in D_{Fe} and ν_{Fe} in the RMP phase can account for the main features of the decrease of iron spatial profiles. EMC3-EIRENE numerical modelling with RMP geometry and high-Z impurities has been carried out predicting impurity screening effects near the divertor region for low-Z impurities in an RMP phase. The overall suppression of tungsten ions and exhaust of C^{6+} ions toward the SOL are confirmed by observations with EUV spectroscopy.

Declaration of interests

The authors report no conflict of interest.

REFERENCES

CUI, Z. Y., MORITA, S., ZHOU, H. Y., DING, X. T., SUN, P., KOBAYASHI, M., CUI, X. W., XU, Y., HUANG, X. L., SHI, Z. B., *et al.* 2013 Enhancement of edge impurity transport with ECRH in the HL-2A tokamak. *Nucl. Fusion* **53**, 093001.

DAI, S. Y., KOBAYASHI, M., KAWAMURA, G., MORITA, S., ZHANG, H., OISHI, T., FENG, Y., WANG D. Z., SUZUKI, Y. & LHD EXPERIMENTAL GROUP 2016 EMC3-EIRENE modelling of edge impurity transport in the stochastic layer of the large helical device compared with extreme ultraviolet emission measurements. *Nucl. Fusion* **56**, 066005.

DAI, S. Y., ZHANG, H. M., LYU, B., WANG, L., FENG, Y., WANG, Z. X. & WANG, D. Z. 2020 Impacts of resonant magnetic perturbations on edge carbon transport and emission on EAST with EMC3-EIRENE modelling. *J. Plasma Phys.* **86**, 815860303.

DUX, R. 2014 STRAHL user manual. *Tech. Report* IPP 10/30. http://hdl.handle.net/11858/00-001M-0000-0027-0DB8-4.

EVANS, T. E., MOYER, R. A., THOMAS, P. R., WATKINS, J. G., OSBORNE, T. H., BOEDO, J. A., DOYLE, E. J., FERNSTERMACHER, M. E., FINKEN, K. H., GROEBNER, R. J., *et al.* 2004 Suppression of large edge-localized modes in high-confinement DIII-D plasmas with a stochastic magnetic boundary. *Phys. Rev. Lett.* **92**, 235003.

FENG, Y., SARDEI, F., KISSLINGER, J. & GRIGULL, T. 1997 A 3D Monte Carlo code for plasma transport in island divertors. *J. Nucl. Mater.* **241–243**, 930–934.

FISCHER, R., FUCHS, C., KURZAN, B., MCDERMOTT, R. M., PUTTERICH, T., RATHGEBER, S. K., SUTTROP, W., VIEZZER, E., WILLENSDORFER, M., WOLFRUM, E. *et al.* 2011 Effect of non-axisymmetric magnetic perturbations on profiles at ASDEX Upgrade. In *38th EPS Conference on Plasma Physics*, Strasbourg, France, 27 June–1st July, P1.072.

GREICHE, A., LIANG, Y., MARCHUK, O., BERTSCHINGER, G., BIEL, W., BURHENN, R., DUX, R., KOSLOWSKI, H. R., KRAMER-FLECKEN, A., LOWENBRUCK, K. 2008 Transport of argon and iron during a resonant magnetic perturbation at TEXTOR-DED. *Plasma Phys. Control. Fusion* **51**, 032001.

HIRAI, T., ESCOURBIAC, F., CARPENTIER-CHOUCHANA, S., DUROCHER, A., FEDOSOV, A., FERRAND, L., JOKINEN, T., KOMAROV, V., MEROLA, M., MITTEAU, R., *et al.* 2014 ITER full tungsten divertor qualification program and progress. *Phys. Scr.* **T159**, 014006.

LUNT, T., FENG, Y., BERNERT, M., HERRMANN, A., DE MARNE, P., MCDERMOTT, R., MULLER, H. W., POTZEL S., PUTTERICH, T., RATHGEBER, S. *et al.* 2012 First EMC3-EIRENE simulations of the impact of the edge magnetic perturbations at ASDEX Upgrade compared with the experiment. *Nucl. Fusion* **52**, 054013.

LYU, B., WANG, F. D., PAN, X. Y., CHEN, J., FU, Y., LI, Y. Y., BITTER, M., HILL, K. W., DELGADO-APARICIO, L. F., PABLANT, N. *et al.* 2014 Upgrades of imaging X-ray crystal spectrometers for high-resolution and high-temperature plasma diagnostics on EAST. *Rev. Sci. Instrum.* **85**, 11E406.

LYU, B., CHEN, J., HU, R. J., WANG, F. D., LI, Y. Y., FU, J., SHEN, Y. C., BITTER, M., HILL, K. W., DELGADO-APARICIO, L. F. *et al.* 2016 Measurement of helium-like and hydrogen-like argon spectra using double-crystal X-ray spectrometers on EAST. *Rev. Sci. Instrum.* **87**, 11E326.

MEROLA, M., ESCOURBIAC, F., RAFFRAY, R., CHAPPUIS, P., HIRAI, T. & MARTIN, A. 2014 Overview and status of ITER internal components. *Fusion Engng Des.* **89** (7–8), 890–895.

MORITA, S., DONG, C. F., KOBAYASHI, M., GOTO, M., HUANG, X. L., MURAKAMI, I., OISHI, T., WANG E. H., ASHIKAWA, N., FUJII, K. *et al.* 2013 Effective screening of iron impurities in the ergodic layer of the large helical device with a metallic first wall. *Nucl. Fusion* **53**, 093017.

REITER, D. 1992 Progress in two-dimensional plasma edge modelling. *J. Nucl. Mater.* **196–198**, 80–89.

SCHMITZ, O., IDA, K., KOBAYASHI, M., BADER, A., BREZINSEK, S., EVANS, T. E., FUNABA, H., GOTO M., MITARAI, O., MORISAKI, T., *et al.* 2016 Enhancement of helium exhaust by resonant magnetic perturbation fields at LHD and TEXTOR. *Nucl. Fusion* **56**, 106011.

SHEN, Y., DU, X., ZHANG, W., WANG, Q., LI, Y., FU, J., WANG, F., XU, J., LYU, B., SHI, Y., *et al.* 2013 Space-resolved extreme ultraviolet spectrometer system for impurity behavior research on experimental advanced superconducting tokamak. *Nucl. Instrum. Meth.* A **700**, 86–90.

SHEN, Y., LYU, B., ZHANG, H., LI, Y., FU, J., VOGEL, G., WANG, X., XU, H., WU, D., ZANG, Q., *et al.* 2019 Suppression of molybdenum impurity accumulation in the core using on-axis electron cyclotron resonance heating in EAST. *Phys. Plasmas* **26**, 032507.

SUMMERS, H. P., DICKSON, W. J., O'MULLANE, M. G., BADNELL, N. R., WHHITEFORD, A. D., BROOKS, D. H., LANG, J., LOCH, S. D. & GRIFFIN, D. C. 2006 Ionization state, excited populations and emission of impurities in dynamic finite density plasmas: I. The generalized collisional–radiative model for light elements. *Plasma Phys. Control. Fusion* **48**, 263.

SUN, Y., LIANG, Y., LIU, Y. Q., GU, S., YANG, X., GUO, W., SHI, T., JIA, M., WANG, L., LYU, B., *et al.* 2016 Nonlinear transition from mitigation to suppression of the edge localized mode with resonant magnetic perturbations in the EAST tokamak. *Phys. Rev. Lett*. **117**, 115001.

SUN, Y., LIANG, Y., QIAN, J., SHEN, B. & WAN, B. 2015 Modeling of non-axisymmetric magnetic perturbations in tokamaks. *Plasma Phys. Control. Fusion* **57**, 045003.

VOGEL, G., ZHANG, H., SHEN, Y., SUN, Y. W., ZANG, Q., GU, N., FU, J., CHEN, J., HU, R., LIU, H., *et al.* 2018 Extreme ultraviolet spectroscopy applied to study RMP effects on core impurity concentration in EAST. *IEEE Trans. Plasma Sci*. **46** (5), 1350–1355.

WAN, B., LIANG, Y., GONG, X., LI, J.G., XIANG, N., XU, G.S., SUN, Y. W., WANG, L., QIAN, J., LIU, H., *et al.* 2017 Overview of EAST experiments on the development of high-performance steady-state scenario. *Nucl. Fusion* **57**, 102019.

ZANG, Q., ZHAO, J., YANG, L., HU, Q., JIA, Y., ZHANG, T., XI, X., BHATTI, S. H. & GAO, X. 2010 Development of a Thomson scattering diagnostic system on EAST. *Plasma Sci. Technol.* **12**, 144.

ZHANG, H., MORITA, S., DAI, S., OISHI, T., GOTO, M., HUANG, X., KAWAMURA, G., KOBAYASHI, M., LIU, Y., MURAKAMI, I., *et al.* 2017 Vertical profiles and two-dimensional distributions of carbon line emissions from $C2+-C5+$ ions in attached and RMP-assisted detached plasmas of large helical device. *Phys. Plasmas* **24**, 022510.